



Directional atomic layer etching of MgO-doped lithium niobate using sequential exposures of H₂ and SF₆ plasma

Ivy I. Chen ¹ Jennifer Solgaard,² Ryoto Sekine,² Azmain A. Hossain,¹ Anthony Ardizzi,¹
David S. Catherall,¹ Alireza Marandi,² Frank Greer,³ and Austin J. Minnich ^{1,*}

¹*Division of Engineering and Applied Science,
California Institute of Technology, Pasadena, California 91125, USA*

²*Department of Electrical Engineering,
California Institute of Technology, Pasadena, CA, USA*

³*Jet Propulsion Laboratory, Pasadena, CA, USA*

(Dated: October 17, 2023)

Abstract

Lithium niobate (LiNbO₃, LN) is a ferroelectric crystal of interest for integrated photonics owing to the ability to impart periodic or chirped poling via an external electric field and its large second-order optical nonlinearity compared to other photonic materials like SiN. The introduction of thin-film lithium niobate (TFLN) based on ion-slicing has enabled photonic circuits with improved figures of merit on account of the greater refractive index contrast than is achievable in bulk LN. However, TFLN device performance is presently limited by surface roughness scattering induced by Ar⁺ milling and the lack of adequately precise etch depth control. Atomic layer etching (ALE) could potentially overcome these limitations, but no ALE process has been reported for LN. Here, we report a directional ALE process for x-cut MgO-doped LN using sequential exposures of H₂ and SF₆ plasma. We observe etch rates up to 1.01 ± 0.05 nm/cycle with a synergy of 94%. This process has the potential to serve as a post-processing step to achieve sub-nanometer-scale etch depth control for TFLN devices, which may both increase the photonic performance of existing TFLN devices and ultimately enable novel devices not attainable in other integrated photonic platforms.

* aminnich@caltech.edu

I Introduction

Lithium niobate (LiNbO_3 or LN) is a ferroelectric crystal of interest for a variety of integrated photonics applications ranging from electro-optic modulators in fiber-optic communications to quantum optics.[1] It simultaneously exhibits a number of useful properties for photonics applications, including a large transparency window, wide electro-optic bandwidth, ferroelectric properties, and high second-order nonlinear susceptibility, [2–6] making it an attractive platform compared to those based on other materials like silicon nitride. [1] Early efforts to create on-chip photonic devices involved Ti ion diffusion or proton-exchange on bulk LN wafers to provide the necessary refractive index contrast.[7–12] However, the relatively small refractive index contrast from this approach resulted in weak optical confinement, negatively impacting device performance.

With the development of ion-slicing and wafer bonding processes for LN onto silicon dioxide, [13–15] thin-film lithium niobate (TFLN) wafers have become commercially available, allowing for the realization of dense circuits with tightly-confining waveguides. Devices that have been fabricated on TFLN include record large squeezed states on-chip, [16] > 100 GHz electro-optic modulators with CMOS compatible voltages, [17] broadband frequency comb sources, [18–20] and on-chip mode-locked lasers. [21, 22] Wet and dry etching methods are widely used for pattern transfer, but dry etching is the most common owing to the need for anisotropic etching. [1, 7] Process development for dry etching of LN is more challenging compared to that for other photonic materials such as SiN because LN is a ternary compound. Fluorine- [23] or chlorine- [24] based reactive ion etching (RIE) processes have been reported, but they suffer from redeposition of stable Li compounds such as LiF, leading to an increase in sidewall roughness and scattering loss. [1, 23] Proton-exchanged LN has been noted to have lower LiF redeposition during plasma etching due to lower surface Li content. Deep ($> 1 \mu\text{m}$) fluorine-based etches with less LiF redeposition have been accomplished with proton-exchanged LN. [7, 25–27]

In the device community, physical Ar^+ milling remains the preferred dry etch method used for pattern transfer. However, this method has its own limitations such as low etch selectivity with common lithography resists and non-vertical sidewall angles. [1, 28] Additionally, etch depth tolerances for photonic devices are desired to be $\sim \pm 5$ nm to operate in a regime near the desired group-velocity dispersion (GVD) and group-velocity mismatch

(GVM) values, [29, 30] a tolerance which is difficult to achieve with Ar^+ milling. As a result, various device figures of merit are far from their intrinsic upper limits. For instance, the material-limited quality factor for TFLN micro-ring resonators is estimated to be an order of magnitude higher than that realized in present devices due to losses from surface roughness scattering. [31] Decreasing losses and increasing etch depth precision in TFLN circuits will enable system-level integration of on-chip nonlinear optics and allow for quantum information processing [1].

These challenges could be addressed with improved nanofabrication techniques which offer sub-nanometer-scale etch depth control and surface smoothing. In particular, thermal or plasma-enhanced atomic layer etching (ALE) has demonstrated the etch depth control on the angstrom scale and ability to smooth surfaces to the sub-nanometer scale. [32, 33] ALE consists of sequential, self-limiting surface chemical processes that lead to etch per cycle of around 1 Å. ALE can be anisotropic (directional) or isotropic (thermal or plasma-thermal). [33, 34] Anisotropic ALE is based on surface modification by adsorption of a reactant followed by low-energy ion or neutral atom sputtering. [35, 36] The self-limiting nature of anisotropic ALE is defined by the thickness of the modified surface and the difference in sputtering threshold between the modified and unmodified surface. Thermal (isotropic) ALE is based on a cycle of surface modification and volatilization reactions. Recent developments in ALE have also employed a pulsed-bias approach, where the flow of gases is held constant and the DC bias is turned on and off, resulting in faster ALE cycle times. [37] Thermal and anisotropic ALE recipes have been developed for various semiconductors and dielectrics such as SiO_2 , [38, 39] InP , [40–42] GaAs , [43–46] and Si_3N_4 . [47–52] Surface smoothing due to ALE has been observed for various materials, [32, 53–57] a feature which has been attributed to conformal layer-by-layer removal and curvature-dependent surface modification. [58] However, no ALE processes have been reported for LN.

Here, we report an ALE process for MgO -doped X-cut LN. Using sequential exposures of H_2 and SF_6 , various etch per cycle values (EPC) from 5.4 ± 0.3 Å/cycle to 10.1 ± 0.5 Å/cycle are achieved with synergies ranging from 88 – 94%. We observe the saturation of both half-steps of the process. Although the ALE process increases surface roughness due to LiF and MgF_2 redeposition, we show that the surface can be returned to its original roughness with a subsequent RCA clean. This process has the potential to serve as a post-

processing step to achieve improved etch depth precision within several nanometers of the target value. The use of this process as post-processing step will therefore allow the desired GVM and GVD to be achieved, in turn enabling improved device characteristics such as a larger phase-matching bandwidth or higher efficiency of nonlinear frequency conversion.

II Experimental Methods

The samples consisted of bulk 3-inch 5% mol MgO-doped LN wafers (G & H Photonics). The wafers were diced into $7\text{ mm} \times 7\text{ mm}$ substrates using a Disco DAD 321 dicing saw and then cleaned by sonication in AZ NMP Rinse, acetone, and isopropyl alcohol. The samples were etched in an Oxford Instruments PlasmaPro 100 Cobra system. As shown in Figures 1(A) to 1(D), the process consisted of sequential exposures to H_2 and SF_6 plasmas with purges between each exposure. This process was inspired by the observation that proton-exchanged LN can be etched with fluorine plasmas with reduced LiF redeposition [7, 12, 25–27] and because the same recipe approach successfully achieved quasi-ALE of SiN. [52]

The nominal ALE recipe consists of an 8-second H_2 plasma exposure (300 W ICP power, 50 W RIE power, 205 V DC bias, 50 sccm H_2) followed by a 30-second SF_6 exposure (300 W ICP power, 3 W RIE power, 47 V DC bias, 17 sccm SF_6 , 35 sccm Ar), although variations of the process parameters are possible around these values. 5-second purge times with 40 sccm Ar were used between plasma half-steps. The chamber pressure was set at 10 mTorr and the substrate table temperature was set to 0°C as measured by the table thermometer. The table thermometer was set to 0°C rather than room temperature as straighter sidewall profiles have been reported at lower temperatures. [52]

To measure saturation curves, the chamber pressure and ICP power were kept constant at 10 mTorr and 300 W, respectively, during half-steps, while the exposure time for each half-step was varied. H_2 exposure time was varied from 0 to 60 seconds with SF_6 held at 30 seconds, and SF_6 exposure time was varied from 0 to 40 seconds with H_2 exposure held at 8 seconds. The substrate table temperature was kept constant at 0°C , as measured by the substrate table thermometer. Prior to introducing the sample into the chamber for etching, the chamber walls and blank Si carrier wafer were cleaned by a 30-minute Ar^+ plasma with 1500 W ICP and 100 W RF power followed by a 15-minute O_2/SF_6 plasma with the same power parameters. When the sample was loaded into the chamber, a 3-minute wait time was used before processing to allow the sample to equilibrate with the table. All samples

were etched for 50 cycles unless otherwise noted.

To enable etch depth measurements, step patterns consisting of periodic $400\text{ }\mu\text{m}^2$ squares were written into a resist using photolithography, as shown in Figure 1(E). The pattern was transferred to the +X face of the samples using AZ5214 photoresist and a Heidelberg MLA 150 Maskless Aligner with a dose of $150\text{ mJ}/\text{cm}^2$, followed by development with AZ 300 MF developer. Etch per cycle (EPC) was calculated by measuring the difference in height from etch depth for a processed sample and dividing it by the total number of cycles. The total etch depth was measured using $2.5 \times 10\text{ }\mu\text{m}^2$ AFM scans on a Park Instruments NX atomic force microscope with a non-contact cantilever tip. Scan rate was set to 1 Hz and etch depths were averaged over 5 line profiles in the scan. RMS surface roughness of a reference TFLN Ar^+ milled waveguide sample and power spectral density (PSD) scans were obtained using a Bruker Dimension Icon atomic force microscope (AFM) over a $50 \times 50\text{ nm}^2$ area with a 0.5 Hz scan rate. Sample tilt from all AFM scans were removed via linear plane fit.

X-ray photoelectron spectroscopy (XPS) analysis was performed using a Kratos Axis Ultra x-ray photoelectron spectrometer using a monochromatic Al $\text{K}\alpha$ source. A 1.3 nm thick layer of carbon, as measured by a quartz crystal monitor, was deposited using sputtering to reduce charging effects during scans (Leica EM ACE600 Carbon Evaporator). The resulting data was analyzed in CASA-XPS from Casa Software Ltd. For each sample, we collected the carbon C1s, oxygen O1s, niobium Nb3d5/2 and Nb 3d3/2, niobium Nb 4s, lithium Li1s, fluorine F1s, and magnesium Mg2p peaks. The carbon C1s peak was used as a reference to calibrate peak positions. We fit the data using a Shirley background subtraction and peak fitting routines from Refs. [59, 60].

III Results

Figure 2(A) shows the thickness change of LN versus cycle number for individual half cycles and the overall process. An etch rate of $0.6\text{ }\text{\AA}/\text{cycle}$ is observed for the SF_6 half step. For the H_2 step, a thickness increase was observed, which may be attributed to a volume expansion of the crystal due to H_2 exposure. Such thickness increases for one half-step have been reported in other processes [33]. On the other hand, when using both steps sequentially, an etch rate of $5.4 \pm 0.3\text{ }\text{\AA}/\text{cycle}$ is observed.

To gain more insight into the process and verify its self-limiting nature, we measured saturation curves for each half-cycle. In Figure 2(B), the SF_6 plasma half step is held

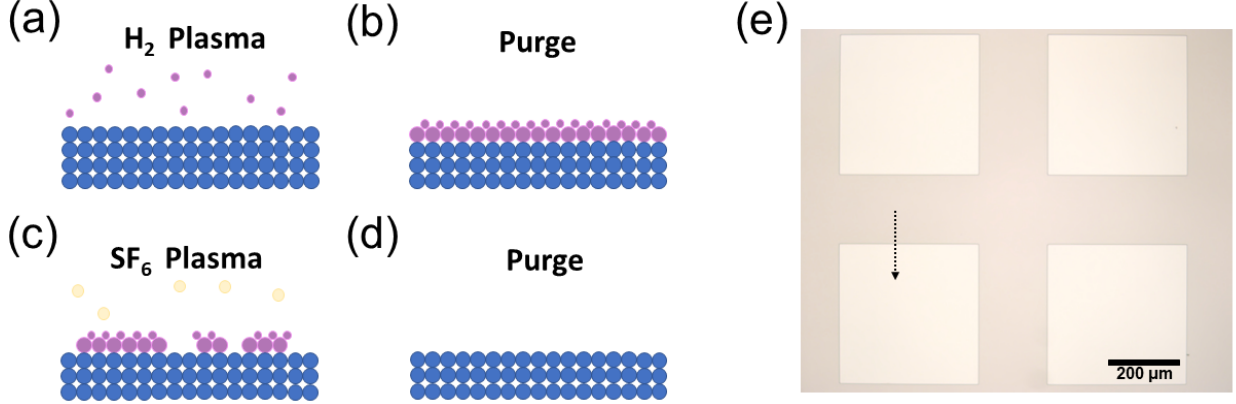


Figure 1. (a-d) ALE process for MgO-doped LN. A hydrogen plasma exposure (pink) leads to a proton-exchanged modified layer (pink circles) at the top of the sample (blue dots), followed by a purge. A subsequent SF_6 plasma exposure (yellow dots) yields volatile Nb, Li, and O species. A final purge completes the cycle. (e) Microscope image ($10\times$ magnification) of the developed lithography pattern on the LN wafer. The dotted line indicates the direction of AFM scan for etch depth measurements.

constant at 30 seconds while the H_2 exposure time is varied from 0 to 30 seconds. Saturation occurs at $10.1 \pm 0.5 \text{ \AA/cycle}$ above 30 seconds H_2 exposure time. In Figure 2(C), the H_2 exposure time is held constant at 8 seconds while the SF_6 exposure time is varied from 0 to 40 seconds. The etch rate saturates at $5.4 \pm 0.3 \text{ \AA/cycle}$ for SF_6 exposure times longer than 30 seconds, indicating that the SF_6 step preferentially etches the hydrogen-modified layer. These observations indicate that both half-steps are self-limiting, implying that the process is indeed atomic layer etching.

The synergy, S , as defined by Ref. [55], quantitatively compares the etch depth using only individual steps of the ALE cycle to the etching obtained with the full etch cycle as $S = (1 - (\alpha + \beta)/\text{EPC}_{\text{cycle}}) \times 100$, where α is the EPC of the H_2 half-cycle, β is the EPC of the SF_6 half-cycle, and $\text{EPC}_{\text{cycle}}$ is the EPC of the full cycle. For the present process in which a thickness increase is observed after H_2 exposure, we calculated the synergy assuming zero EPC for that step. We obtain a synergy value of 88% for the nominal recipe. If we consider a variation of the recipe where the H_2 half step is 30 seconds long, we achieve an EPC of $10.1 \pm 0.5 \text{ \AA/cycle}$ with a synergy of 94%. These synergy values are compatible with typical synergy values reported in Ref. [32].

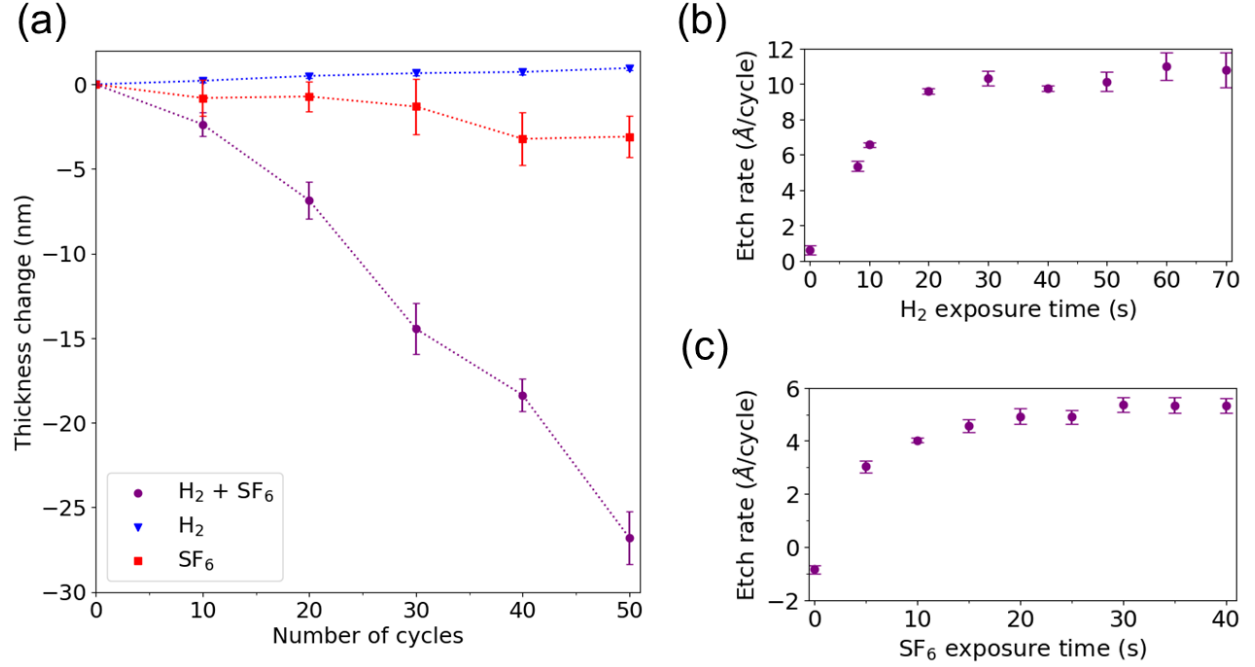


Figure 2. (a) EPC versus cycle number with only H_2 plasma exposure (blue triangles), only SF_6 plasma exposure (red squares), and both half-cycles (purple circles). All processes occur at $0^\circ C$. The dashed lines are guides to the eye. (b) EPC versus H_2 gas exposure time with SF_6 exposure time fixed at 30 s. (c) EPC versus SF_6 exposure time with H_2 exposure time fixed at 8 s. The etch rates are observed to saturate with exposure time, demonstrating the self-limiting nature of the process.

We next characterize the chemical composition of bulk LN before and after 50 cycles ALE using XPS. No depth-profiling XPS is reported due to preferential sputtering of O over Nb with an Ar^+ beam [61], complicating the interpretation of the measurements. The C1s peak at 284.8 eV is used as a reference. In Figures 3(A) to 3(D), we show the core levels of Nb3d, O1s; Nb4s, Li1s, and Mg2p; and F1s, respectively. For the Nb3d XPS spectra in Figure 3(A), we observe a single doublet peak consisting of a $3d_{5/2}$ and $3d_{3/2}$ subpeak corresponding to LN (207.5 eV and 210.3 eV) [62–64]. In Figure 3(B), we report the O1s spectra with two subpeaks at 530.5 and 532.3 eV, corresponding to metal oxide and O-C bonds, respectively [65]. In Figure 3(C), we report the Nb4s, Li1s, and Mg2p spectra at (values are for bulk LN) 60.4 eV, 55.6 eV, and 50.8 eV, respectively [64, 65]. The Li1s peak energy agrees well with reported binding energies for LiF [65, 66]. After ALE, there is a

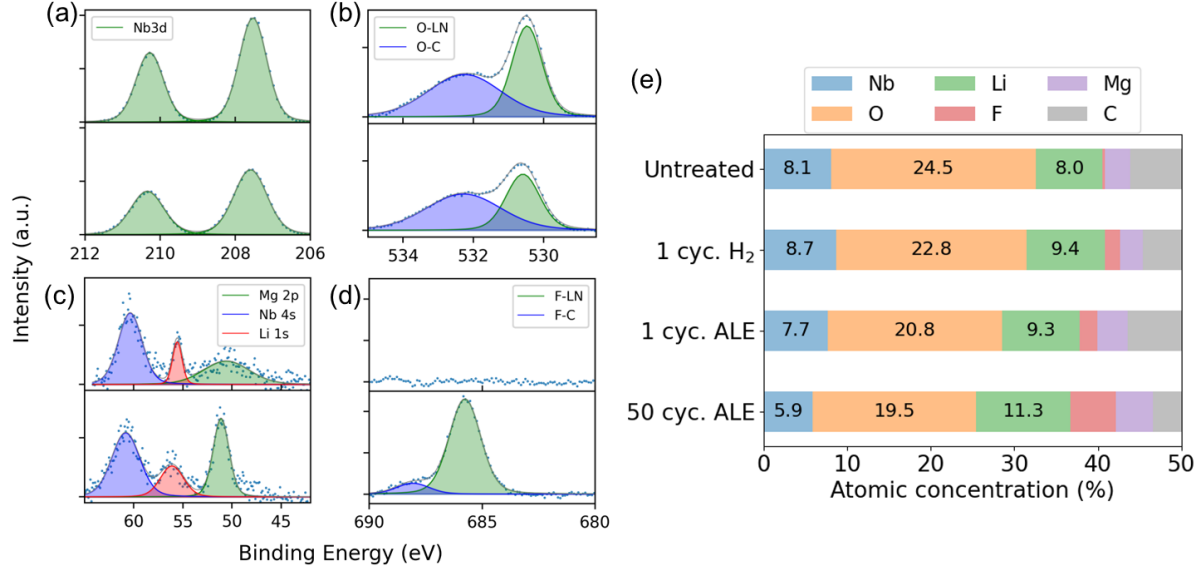


Figure 3. Surface XPS spectra showing (a) Nb3d, (b) O1s, (c) Nb4s, Li1s, Mg2p and (d) F1s spectra. The spectra is shown for (top) original and (bottom) etched bulk MgO-doped LN over 50 cycles. The measured (blue dots) and fit spectra (gray lines) intensity are reported in arbitrary units (a.u.) against the binding energy on the x-axis. (e) Surface atomic concentration obtained from XPS spectra for untreated bulk LN, 1 cycle H₂ exposure, 1 full cycle, and 50 cycles. Due to the conductive carbon coating, roughly 55% of the atomic concentration in the sample surface consists of carbon. The plot is truncated at 50% to highlight the concentration of non-carbon species.

broadening of the Li1s peak and a slight shift toward higher binding energies for Nb4s, Li1s, and Mg2p peaks. In Figure 3(D), we report the F1s spectra with two subpeaks at 685.8 eV and 688.1 eV corresponding to LiF and F-C bonds, respectively [64–66]. After ALE, we observe slight shifts in binding energies for the Nb, Li1s, and Mg2p peaks to higher binding energies corresponding to fluoride bond formation. There is also an increased concentration of Mg after ALE, suggesting that MgF₂ is also formed.

In Figure 3(E), we report the atomic concentrations of Nb, Li, Mg, O, F, and C obtained from the XPS data at various stages of the process. Due to the carbon coating used in XPS, the carbon content of the surface is estimated to be about 55% in each sample. In the untreated bulk sample, the atomic concentrations are found to be 8.1% Nb, 24.5% O, 8% Li, 3.1% Mg, and 0.2% F. With one H₂ cycle exposure, the atomic concentrations are 8.7% Nb, 22.8% O, 9.4% Li, 2.8% Mg, and 1.8% F. The presence of fluorine is likely from residual

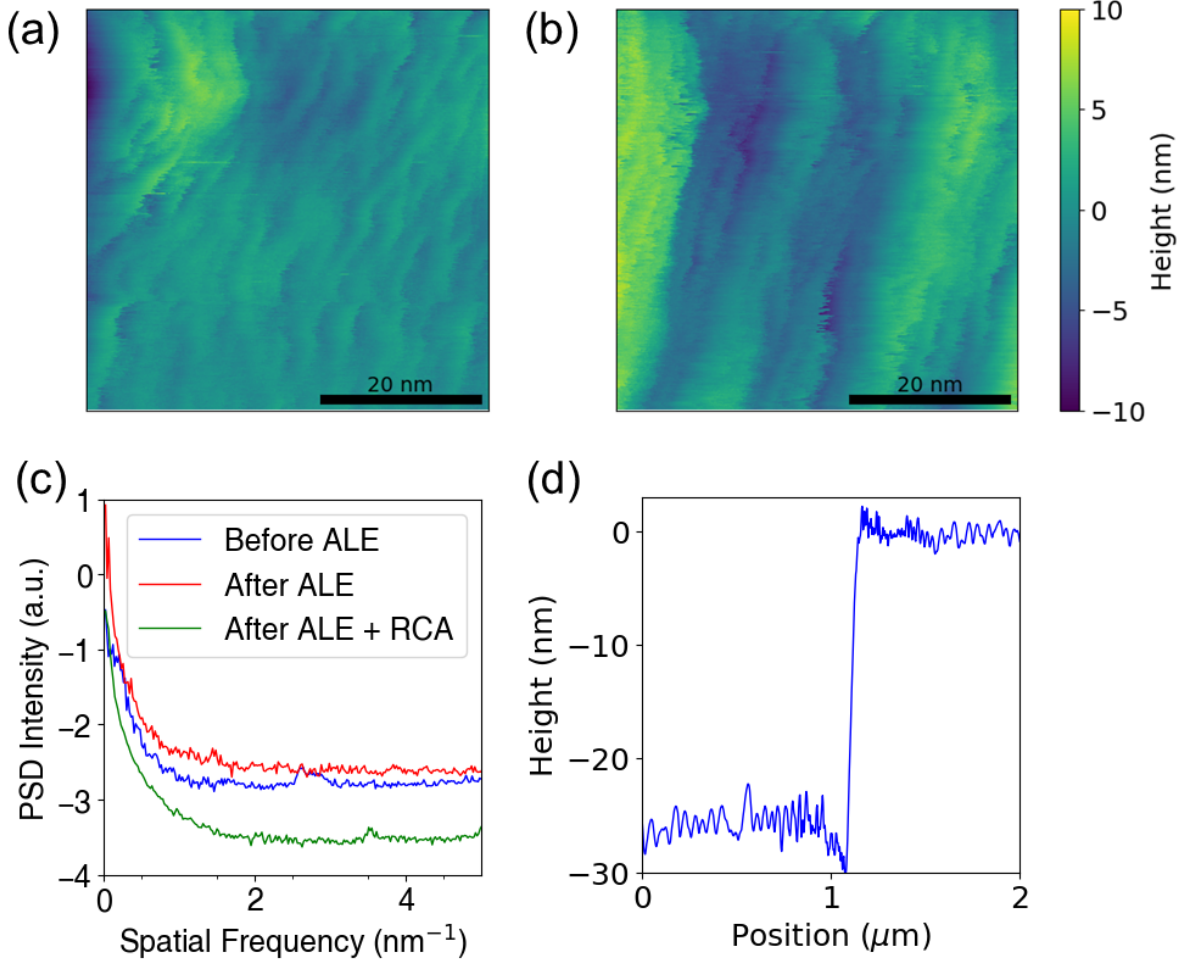


Figure 4. AFM scan showing height-maps of TFLN waveguide sidewall with linear-plane tilt removal before (a) and after 50 ALE cycles (b). (c) Height-map PSD of the samples before ALE, after 50 cycles ALE, and after 50 cycles ALE and an RCA clean. (d) AFM line scan of the step pattern after 50 cycles of ALE, indicating the occurrence of microtrenching and supporting the directional nature of the process.

fluorine on the chamber walls after the chamber clean. Lithium content on the surface is observed to increase after 1 H_2 half-cycle, indicating that some LiF redeposition is occurring despite the H_2 plasma exposure. Bulk LN with 1 cycle of ALE has atomic concentrations of 7.7% Nb, 20.8% O, 9.3% Li, 3.6% Mg, and 2.2% F. After 50 cycles of ALE, the atomic concentrations are 5.9% Nb, 19.5% O, 11.3% Li, 4.4% Mg, and 5.5% F. The data suggests that the presence of fluorine compounds, specifically LiF and MgF_2 , increases with cycle number, while Nb and O are preferentially etched.

We next characterized the effect of ALE on the surface roughness of TFLN samples.

For these measurements, we used additional samples consisting of TFLN with Ar^+ milled waveguides that were smoothed post-etch with an HF dip and RCA clean, corresponding to the standard process for TFLN device fabrication [1, 28]. Using AFM scans, the initial RMS sidewall roughness is measured to be 1.75 ± 0.80 nm and an average roughness of 1.25 ± 0.60 nm. After applying 50 cycles, R_q and R_a are measured to be 3.1 ± 0.55 nm and 2.61 ± 0.56 nm, respectively. We also observe an increase in PSD intensity over all length scales from 0 to 5 nm after ALE. Figures 4(A) and 4(B) shows the plane-fit height map of Ar^+ etched sidewall before and after 50 cycles of ALE at 0°C respectively. Figure 4(C) shows the PSD curves before and after ALE. Surface roughening is observed in bulk samples as well (not shown).

Despite this increase in roughness after ALE, the sample can be returned to its pre-ALE surface roughness by an RCA clean. We performed a second RCA clean following ALE of the sample. The measured R_q and R_a are 0.86 ± 0.50 nm and 0.59 ± 0.41 nm, respectively. Figure 4(C) shows that after the RCA clean, the roughness over all length scales from 0 to 5 nm is reduced past the original roughness fabricated by Ar^+ milling and subsequent smoothing. These observations suggest that the roughness induced by the ALE process is from redeposition of LiF and MgF_2 and that it can be mitigated using the standard procedure already in use for TFLN device fabrication.

Figure 4(D) shows an AFM line scan of the step pattern on bulk LN after 50 cycles of ALE. We observe some microtrenching at the base of the sidewall, where there is a deeper etch at the base of the step compared to regions farther from the step. Microtrenching is commonly found after directional etches originating from ion reflection from sidewalls and is also observed in Ar^+ milled TFLN. The profile is consistent with the directional nature of the process.

IV Discussion

Our ALE process may find potential applications in the fabrication of TFLN devices to achieve precise etch depths through the self-limiting process. The nominal poling period for quasi-phase-matching critically depends on the waveguide geometry such as top width, etch depth, and the total LN film thickness. [18] The present process could be used after Ar^+ milling to obtain etch depths within the desired group-velocity mismatch and group-velocity dispersion regimes. The uncertainty in etch depth is governed by the increase in roughness

from LiF redeposition as the number of ALE cycles increase. In addition, the increase in roughness during ALE can be mitigated with an RCA clean. The ALE system in our work (Oxford Instruments, Plasma Pro 100 Cobra) is able to process 200 mm diameter substrates, and therefore our process has the potential to extend to wafer-scale applications.

Future work may focus on surface smoothing through reducing LiF formation by increasing the H_2 concentration at the surface and lowering the RF bias on the SF_6 half step. Development of an in-situ gas-based LiF removal process may enable ALE without the need for a subsequent RCA clean. Additionally, faster saturation may be achieved by increasing ICP or chamber pressure. The dependence of sidewall angle on substrate table temperature is another topic of interest. The hydrogen modification step may also allow for ALE using chlorine-based plasmas, which would be compatible with hydrogen silsesquioxane (HSQ), a preferred etch mask for TFLN fabrication. Additionally, LiCl is more volatile than LiF and increases in surface roughness due to redeposition may be avoided.

V Conclusion

We have reported an ALE process consisting of sequential exposures of hydrogen and SF_6 plasma for X-cut MgO-doped lithium niobate that is compatible with low-pressure ICP RIE systems. We observe etch rates up to $10.1 \pm 0.5 \text{ \AA/cycle}$ with a synergy of up to 94%. Both half-steps of the recipe showed saturation with respect to exposure time. Despite the occurrence of LiF redeposition leading to increased roughness after ALE, the sample roughness can be returned to its original value by an RCA clean. The ALE and post-process RCA clean can together be used to achieve etch depth control within $\sim \pm 5 \text{ nm}$ without increasing sidewall roughness. This ability is expected to enable improved TFLN device performance and potential functionalities which are not achievable in other integrated photonics platforms.

VI Acknowledgements

This work was supported by NSF under Award #2234390. This research was primarily carried out at the Microdevices Laboratory (MDL) Jet Propulsion Laboratory (JPL), California Institute of Technology, and in part, carried out at the California Institute of Technology. We gratefully acknowledge the critical support and infrastructure provided for this work by The Kavli Nanoscience Institute and the Molecular Materials Research Center of the Beck-

man Institute at the California Institute of Technology. The authors thank Russ Renzas for useful discussions.

VII References

- [1] Di Zhu, Linbo Shao, Mengjie Yu, Rebecca Cheng, Boris Desiatov, C. J. Xin, Yaowen Hu, Jeffrey Holzgrafe, Soumya Ghosh, Amirhassan Shams-Ansari, Eric Puma, Neil Sinclair, Christian Reimer, Mian Zhang, and Marko Lončar. Integrated photonics on thin-film lithium niobate. *Adv. Opt. Photon.*, 13(2):242–352, Jun 2021. URL <https://opg.optica.org/aop/abstract.cfm?URI=aop-13-2-242>.
- [2] R. S. Weis and T. K. Gaylord. Lithium niobate: Summary of physical properties and crystal structure. *Applied Physics A*, 37(4):191–203, Aug 01, 1985. ISSN 1432-0630. URL <https://doi.org/10.1007/BF00614817>.
- [3] Ka-Kha Wong. *Properties of lithium niobate*. Number 28. IET, 2002.
- [4] Yongfa Kong, Fang Bo, Weiwei Wang, Dahuai Zheng, Hongde Liu, Guoquan Zhang, Romano Rupp, and Jingjun Xu. Recent progress in lithium niobate: optical damage, defect simulation, and on-chip devices. *Advanced Materials*, 32(3):1806452, 2020.
- [5] Tatyana Volk and Manfred Wöhlecke. *Lithium niobate: defects, photorefractive and ferroelectric switching*, volume 115. Springer Science & Business Media, 2008.
- [6] Luis Arizmendi. Photonic applications of lithium niobate crystals. *physica status solidi (a)*, 201(2):253–283, 2004.
- [7] H. Hu, A. P. Milenin, R. B. Wehrspohn, H. Hermann, and W. Sohler. Plasma etching of proton-exchanged lithium niobate. *Journal of Vacuum Science & Technology A*, 24(4):1012–1015, 06 2006. ISSN 0734-2101. URL <https://doi.org/10.1116/1.2207150>.
- [8] O. Espeso, G. Garcia, A. Climent, F. Agullo-Lopez, G. de la Paliza, J. M. Cabrera, and T. Sajavaara. H–Li correlation and stoichiometry of mixed phases in proton-exchanged LiNbO₃ waveguides. *Journal of Applied Physics*, 94(12):7710–7718, 12 2003. ISSN 0021-8979. URL <https://doi.org/10.1063/1.1626802>.
- [9] J.M. Cabrera, J. Olivares, M. Carrascosa, J. Rams, R. Müller, and E. Diéguez. Hydrogen in lithium niobate. *Advances in Physics*, 45(5):349–392, 1996. URL <https://doi.org/10.1080/00018739600101517>.

- [10] Lars Dörrer, Philipp Tuchel, Erwin Hüger, René Heller, and Harald Schmidt. Hydrogen diffusion in proton-exchanged lithium niobate single crystals. *Journal of Applied Physics*, 129(13): 135105, 04 2021. ISSN 0021-8979. URL <https://doi.org/10.1063/5.0047606>.
- [11] Lutong Cai, Yun Kang, and Hui Hu. Electric-optical property of the proton exchanged phase modulator in single-crystal lithium niobate thin film. *Opt. Express*, 24(5):4640–4647, Mar 2016. URL <https://opg.optica.org/oe/abstract.cfm?URI=oe-24-5-4640>.
- [12] Z. Ren, P. J. Heard, and S. Yu. Proton exchange and diffusion in LiNbO₃ using inductance coupled high density plasma. *Journal of Vacuum Science & Technology B: Microelectronics and Nanometer Structures Processing, Measurement, and Phenomena*, 25(4):1161–1165, 06 2007. ISSN 1071-1023. URL <https://doi.org/10.1116/1.2746052>.
- [13] M. Levy, Jr. Osgood, R. M., R. Liu, L. E. Cross, III Cargill, G. S., A. Kumar, and H. Bakhru. Fabrication of single-crystal lithium niobate films by crystal ion slicing. *Applied Physics Letters*, 73(16):2293–2295, 10 1998. ISSN 0003-6951. URL <https://doi.org/10.1063/1.121801>.
- [14] Miguel Levy and Richard M Osgood. Crystal ion-slicing of single-crystal films, Sep 2000.
- [15] Payam Rabiei and Peter Gunter. Optical and electro-optical properties of submicrometer lithium niobate slab waveguides prepared by crystal ion slicing and wafer bonding. *Applied Physics Letters*, 85(20):4603–4605, 11 2004. ISSN 0003-6951. URL <https://doi.org/10.1063/1.1819527>.
- [16] Rajveer Nehra, Ryoto Sekine, Luis Ledezma, Qiushi Guo, Robert M. Gray, Arkadev Roy, and Alireza Marandi. Few-cycle vacuum squeezing in nanophotonics. *Science*, 377(6612): 1333–1337, 2022. URL <https://www.science.org/doi/abs/10.1126/science.abo6213>.
- [17] Cheng Wang, Mian Zhang, Xi Chen, Maxime Bertrand, Amirhassan Shams-Ansari, Sethumadhavan Chandrasekhar, Peter Winzer, and Marko Lončar. Integrated lithium niobate electro-optic modulators operating at cmos-compatible voltages. *Nature*, 562(7725):101–104, Oct 01, 2018. ISSN 1476-4687. URL <https://doi.org/10.1038/s41586-018-0551-y>.
- [18] Ryoto Sekine, Robert M. Gray, Luis Ledezma, Selina Zhou, Qiushi Guo, and Alireza Marandi. Multi-octave frequency comb from an ultra-low-threshold nanophotonic parametric oscillator, 2023.
- [19] Tsung-Han Wu, Luis Ledezma, Connor Fredrick, Pooja Sekhar, Ryoto Sekine, Qiushi Guo, Ryan M. Briggs, Alireza Marandi, and Scott A. Diddams. Visible to ultraviolet frequency comb generation in lithium niobate nanophotonic waveguides, 2023.

- [20] Marc Jankowski, Carsten Langrock, Boris Desiatov, Alireza Marandi, Cheng Wang, Mian Zhang, Christopher R. Phillips, Marko Lončar, and M. M. Fejer. Ultrabroadband nonlinear optics in nanophotonic periodically poled lithium niobate waveguides. *Optica*, 7(1):40–46, Jan 2020. URL <https://opg.optica.org/optica/abstract.cfm?URI=optica-7-1-40>.
- [21] Mengjie Yu, David Barton III, Rebecca Cheng, Christian Reimer, Prashanta Kharel, Lingyan He, Linbo Shao, Di Zhu, Yaowen Hu, Hannah R. Grant, Leif Johansson, Yoshitomo Okawachi, Alexander L. Gaeta, Mian Zhang, and Marko Lončar. Integrated femtosecond pulse generator on thin-film lithium niobate. *Nature*, 612(7939):252–258, Dec 01, 2022. ISSN 1476-4687. URL <https://doi.org/10.1038/s41586-022-05345-1>.
- [22] Qiushi Guo, Ryoto Sekine, James A. Williams, Benjamin K. Gutierrez, Robert M. Gray, Luis Ledezma, Luis Costa, Arkadev Roy, Selina Zhou, Mingchen Liu, and Alireza Marandi. Mode-locked laser in nanophotonic lithium niobate, 2023.
- [23] H. Hu, A. P. Milenin, R. B. Wehrspohn, H. Hermann, and W. Sohler. Plasma etching of proton-exchanged lithium niobate. *Journal of Vacuum Science & Technology A*, 24(4):1012–1015, 06 2006. ISSN 0734-2101. URL <https://doi.org/10.1116/1.2207150>.
- [24] Mohamed Mahmoud, Lutong Cai, Christian Bottenfield, and Gianluca Piazza. Lithium niobate electro-optic racetrack modulator etched in y-cut lnoi platform. *IEEE Photonics Journal*, 10(1):1–10, 2018.
- [25] Deng Jun, Jia Wei, Ching Eng Png, Si Guangyuan, Jaesung Son, Hyunsoo Yang, and Aaron J. Danner. Deep anisotropic LiNbO₃ etching with SF₆/Ar inductively coupled plasmas. *Journal of Vacuum Science & Technology B*, 30(1):011208, 01 2012. ISSN 2166-2746. URL <https://doi.org/10.1116/1.3674282>.
- [26] Z. Ren, P. J. Heard, J. M. Marshall, P. A. Thomas, and S. Yu. Etching characteristics of LiNbO₃ in reactive ion etching and inductively coupled plasma. *Journal of Applied Physics*, 103(3):034109, 02 2008. ISSN 0021-8979. URL <https://doi.org/10.1063/1.2838180>.
- [27] Arjun Aryal, Isaac Stricklin, Mahmoud Behzadizad, Darren W. Branch, Aleem Siddiqui, and Tito Busani. High-quality dry etching of linbo3 assisted by proton substitution through h2-plasma surface treatment. *Nanomaterials*, 12(16), 2022. ISSN 2079-4991. URL <https://www.mdpi.com/2079-4991/12/16/2836>.
- [28] G. Ulliac, V. Calero, A. Ndao, F.I. Baida, and M.-P. Bernal. Argon plasma inductively coupled plasma reactive ion etching study for smooth sidewall thin film lithium niobate

- waveguide application. *Optical Materials*, 53:1–5, 2016. ISSN 0925-3467. URL <https://www.sciencedirect.com/science/article/pii/S0925346715301816>.
- [29] Luis Ledezma, Ryoto Sekine, Qiushi Guo, Rajveer Nehra, Saman Jahani, and Alireza Marandi. Intense optical parametric amplification in dispersion-engineered nanophotonic lithium niobate waveguides. *Optica*, 9(3):303–308, Mar 2022. URL <https://opg.optica.org/optica/abstract.cfm?URI=optica-9-3-303>.
- [30] Marc Jankowski, Carsten Langrock, Boris Desiatov, Alireza Marandi, Cheng Wang, Mian Zhang, Christopher R. Phillips, Marko Lončar, and M. M. Fejer. Ultrabroadband nonlinear optics in nanophotonic periodically poled lithium niobate waveguides. *Optica*, 7(1):40–46, Jan 2020. URL <https://opg.optica.org/optica/abstract.cfm?URI=optica-7-1-40>.
- [31] Amirhassan Shams-Ansari, Guanhao Huang, Lingyan He, Zihan Li, Jeffrey Holzgrafe, Marc Jankowski, Mikhail Churaev, Prashanta Kharel, Rebecca Cheng, Di Zhu, Neil Sinclair, Boris Desiatov, Mian Zhang, Tobias J. Kippenberg, and Marko Lončar. Reduced material loss in thin-film lithium niobate waveguides. *APL Photonics*, 7(8):081301, 08 2022. ISSN 2378-0967. URL <https://doi.org/10.1063/5.0095146>.
- [32] Keren J. Kanarik, Samantha Tan, and Richard A. Gottscho. Atomic layer etching: Rethinking the art of etch. *The Journal of Physical Chemistry Letters*, 9(16):4814–4821, 2018. URL <https://doi.org/10.1021/acs.jpcllett.8b00997>. PMID: 30095919.
- [33] Steven M. George. Mechanisms of thermal atomic layer etching. *Accounts of Chemical Research*, 53(6):1151–1160, 2020. URL <https://doi.org/10.1021/acs.accounts.0c00084>. PMID: 32476413.
- [34] Keren J. Kanarik, Thorsten Lill, Eric A. Hudson, Saravanapriyan Sriraman, Samantha Tan, Jeffrey Marks, Vahid Vahedi, and Richard A. Gottscho. Overview of atomic layer etching in the semiconductor industry. *Journal of Vacuum Science & Technology A*, 33(2):020802, 03 2015. ISSN 0734-2101. URL <https://doi.org/10.1116/1.4913379>.
- [35] Y. Horiike, T. Tanaka, M. Nakano, S. Iseda, H. Sakaue, A. Nagata, H. Shindo, S. Miyazaki, and M. Hirose. Digital chemical vapor deposition and etching technologies for semiconductor processing. *Journal of Vacuum Science & Technology A*, 8(3):1844–1850, 05 1990. ISSN 0734-2101. URL <https://doi.org/10.1116/1.576814>.
- [36] Keren J. Kanarik, Thorsten Lill, Eric A. Hudson, Saravanapriyan Sriraman, Samantha Tan, Jeffrey Marks, Vahid Vahedi, and Richard A. Gottscho. Overview of atomic layer etching in

- the semiconductor industry. *Journal of Vacuum Science & Technology A*, 33(2):020802, 03 2015. ISSN 0734-2101. URL <https://doi.org/10.1116/1.4913379>.
- [37] J. A. Michaels, N. Deegan, Y. Tsaturyan, J. R. Renzas, D. D. Awschalom, J. G. Eden, and F. J. Heremans. Bias-pulsed atomic layer etching of 4H-silicon carbide producing subangstrom surface roughness. *Journal of Vacuum Science & Technology A*, 41(3):032607, 05 2023. ISSN 0734-2101. URL <https://doi.org/10.1116/6.0002447>.
- [38] Jaime W. DuMont, Amy E. Marquardt, Austin M. Cano, and Steven M. George. Thermal atomic layer etching of sio₂ by a “conversion-etch” mechanism using sequential reactions of trimethylaluminum and hydrogen fluoride. *ACS Applied Materials & Interfaces*, 9(11):10296–10307, 2017. URL <https://doi.org/10.1021/acsami.7b01259>. PMID: 28240864.
- [39] Rezwanur Rahman, Eric C. Mattson, Joseph P. Klesko, Aaron Dangerfield, Sandrine Rivillon-Amy, David C. Smith, Dennis Hausmann, and Yves J. Chabal. Thermal atomic layer etching of silica and alumina thin films using trimethylaluminum with hydrogen fluoride or fluoroform. *ACS Applied Materials & Interfaces*, 10(37):31784–31794, 2018. URL <https://doi.org/10.1021/acsami.8b10899>. PMID: 30179460.
- [40] K. K. Ko and S. W. Pang. Controllable layer-by-layer etching of III–V compound semiconductors with an electron cyclotron resonance source. *Journal of Vacuum Science & Technology B: Microelectronics and Nanometer Structures Processing, Measurement, and Phenomena*, 11(6):2275–2279, 11 1993. ISSN 1071-1023. URL <https://doi.org/10.1116/1.586889>.
- [41] S. D. Park, C. K. Oh, J. W. Bae, G. Y. Yeom, T. W. Kim, J. I. Song, and J. H. Jang. Atomic layer etching of InP using a low angle forward reflected Ne neutral beam. *Applied Physics Letters*, 89(4):043109, 07 2006. ISSN 0003-6951. URL <https://doi.org/10.1063/1.2221504>.
- [42] S. D. Park, C. K. Oh, W. S. Lim, H. C. Lee, J. W. Bae, G. Y. Yeom, T. W. Kim, J. I. Song, and J. H. Jang. Highly selective and low damage atomic layer etching of InP//InAlAs heterostructures for high electron mobility transistor fabrication. *Applied Physics Letters*, 91(1):013110, 07 2007. ISSN 0003-6951. URL <https://doi.org/10.1063/1.2754636>.
- [43] Wenjie Lu, Younghee Lee, Jonas C. Gertsch, Jessica A. Murdzek, Andrew S. Cavanagh, Lisa Kong, Jesús A. del Alamo, and Steven M. George. In situ thermal atomic layer etching for sub-5 nm ingaas multigate mosfets. *Nano Letters*, 19(8):5159–5166, 2019. URL <https://doi.org/10.1021/acs.nanolett.9b01525>. PMID: 31251069.

- [44] T. Meguro, M. Ishii, T. Sugano, K. Gamo, and Y. Aoyagi. Control of the etching reaction of digital etching using tunable uv laser irradiation. *Applied Surface Science*, 82-83:193–199, 1994. ISSN 0169-4332. URL <https://www.sciencedirect.com/science/article/pii/016943329490216X>.
- [45] Yoshinobu Aoyagi, Kohji Shinmura, Kiyoshi Kawasaki, Tomoko Tanaka, Kenji Gamo, Susumu Namba, and Ichirou Nakamoto. Molecular layer etching of GaAs. *Applied Physics Letters*, 60(8):968–970, 02 1992. ISSN 0003-6951. URL <https://doi.org/10.1063/1.106477>.
- [46] Mohammad R. Aziziyan, Hemant Sharma, and Jan J. Dubowski. Photo-atomic layer etching of gaas/algaas nanoheterostructures. *ACS Applied Materials & Interfaces*, 11(19):17968–17978, May 15, 2019. ISSN 1944-8244. URL <https://doi.org/10.1021/acsami.9b02079>.
- [47] Chen Li, Dominik Metzler, Chiukin Steven Lai, Eric A. Hudson, and Gottlieb S. Oehrlein. Fluorocarbon based atomic layer etching of Si₃N₄ and etching selectivity of SiO₂ over Si₃N₄. *Journal of Vacuum Science & Technology A*, 34(4):041307, 07 2016. ISSN 0734-2101. URL <https://doi.org/10.1116/1.4954961>.
- [48] Aziz I. Abdulagatov and Steven M. George. Thermal atomic layer etching of silicon nitride using an oxidation and “conversion etch” mechanism. *Journal of Vacuum Science & Technology A*, 38(2):022607, 02 2020. ISSN 0734-2101. URL <https://doi.org/10.1116/1.5140481>.
- [49] Yohei Ishii, Kazumasa Okuma, Tiffany Saldana, Kenji Maeda, Nobuyuki Negishi, and Jim Manos. Atomic layer etching of silicon nitride using cyclic process with hydrofluorocarbon chemistry. *Japanese Journal of Applied Physics*, 56(6S2):06HB07, may 2017. URL <https://dx.doi.org/10.7567/JJAP.56.06HB07>.
- [50] Sonam D. Sherpa and Alok Ranjan. Quasi-atomic layer etching of silicon nitride. *Journal of Vacuum Science & Technology A*, 35(1):01A102, 11 2016. ISSN 0734-2101. URL <https://doi.org/10.1116/1.4967236>.
- [51] Takashi Matsuura, Yasuhiko Honda, and Junichi Murota. Atomic-order layer-by-layer role-share etching of silicon nitride using an electron cyclotron resonance plasma. *Applied Physics Letters*, 74(23):3573–3575, 06 1999. ISSN 0003-6951. URL <https://doi.org/10.1063/1.124165>.
- [52] Daniel N. Shanks, Rania K. Ahmed, John D. Femi-Oyetoro, Matthew R. Dickie, Andrew D. Beyer, and Frank Greer. Quasiatomic layer etching of silicon nitride enhanced by low temperature. *Journal of Vacuum Science & Technology A*, 41(5):052601, 08 2023. ISSN 0734-2101.

- URL <https://doi.org/10.1116/6.0002846>.
- [53] David R. Zywotko, Jacques Faguet, and Steven M. George. Rapid atomic layer etching of Al₂O₃ using sequential exposures of hydrogen fluoride and trimethylaluminum with no purging. *Journal of Vacuum Science & Technology A*, 36(6):061508, 10 2018. ISSN 0734-2101. URL <https://doi.org/10.1116/1.5043488>.
 - [54] Tomihito Ohba, Wenbing Yang, Samantha Tan, Keren J Kanarik, and Kazuo Nojiri. Atomic layer etching of gan and algan using directional plasma-enhanced approach. *Japanese Journal of Applied Physics*, 56(6S2):06HB06, 2017.
 - [55] Keren J. Kanarik, Samantha Tan, Wenbing Yang, Taeseung Kim, Thorsten Lill, Alexander Kabansky, Eric A. Hudson, Tomihito Ohba, Kazuo Nojiri, Jengyi Yu, Rich Wise, Ivan L. Berry, Yang Pan, Jeffrey Marks, and Richard A. Gottscho. Predicting synergy in atomic layer etching. *Journal of Vacuum Science & Technology A*, 35(5):05C302, 03 2017. ISSN 0734-2101. URL <https://doi.org/10.1116/1.4979019>.
 - [56] Azmain A. Hossain, Haozhe Wang, David S. Catherall, Martin Leung, Harm C. M. Knoops, James R. Renzas, and Austin J. Minnich. Isotropic plasma-thermal atomic layer etching of superconducting titanium nitride films using sequential exposures of molecular oxygen and SF₆/H₂ plasma. *Journal of Vacuum Science & Technology A*, 41(6):062601, 09 2023. ISSN 0734-2101. URL <https://doi.org/10.1116/6.0002965>.
 - [57] Haozhe Wang, Azmain Hossain, David Catherall, and Austin J. Minnich. Isotropic plasma-thermal atomic layer etching of aluminum nitride using SF₆ plasma and Al(CH₃)₃. *Journal of Vacuum Science & Technology A*, 41(3):032606, 05 2023. ISSN 0734-2101. URL <https://doi.org/10.1116/6.0002476>.
 - [58] Sven H. Gerritsen, Nicholas J. Chittock, Vincent Vandalon, Marcel A. Verheijen, Harm C. M. Knoops, Wilhelmus M. M. Kessels, and Adriaan J. M. Mackus. Surface smoothing by atomic layer deposition and etching for the fabrication of nanodevices. *ACS Applied Nano Materials*, 5(12):18116–18126, 2022. URL <https://doi.org/10.1021/acsanm.2c04025>.
 - [59] H. Turčičová, J. Zemek, J. Tóth, and I. Drbohlav. Single-crystal linbo₃ surfaces processed in low-temperature hydrogen plasma: Xps, reels and afm study. *Surface and Interface Analysis*, 34(1):468–471, 2002. URL <https://analyticalsciencejournals.onlinelibrary.wiley.com/doi/abs/10.1002/sia.1340>.

- [60] Rachel G. Gruenke, Oliver A. Hitchcock, E. Alex Wollack, Christopher J. Sarabalis, Marc Jankowski, Timothy P. McKenna, Nathan R. Lee, and Amir H. Safavi-Naeini. Surface modification and coherence in lithium niobate saw resonators, 2023.
- [61] P. C. Karulkar. Effects of sputtering on the surface composition of niobium oxides. *Journal of Vacuum Science and Technology*, 18(2):169–174, 03 1981. ISSN 0022-5355. URL <https://doi.org/10.1116/1.570717>.
- [62] N. Kaufherr, D. J. Eichorst, and D. A. Payne. X-ray photoelectron spectroscopy studies of alkoxide-derived lithium niobate. *Journal of Vacuum Science & Technology A*, 14(2):299–305, 03 1996. ISSN 0734-2101. URL <https://doi.org/10.1116/1.579892>.
- [63] NIST X ray Photoelectron Spectroscopy Database. Nist standard reference database number 20, national institute of standards and technology. *Gaithersburg MD*, page 20899, 2000.
- [64] E.A. Skryleva, I.V. Kubasov, Ph.V. Kiryukhantsev-Korneev, B.R. Senatulin, R.N. Zhukov, K.V. Zakutailov, M.D. Malinkovich, and Yu.N. Parkhomenko. Xps study of li/nb ratio in linbo3 crystals. effect of polarity and mechanical processing on linbo3 surface chemical composition. *Applied Surface Science*, 389:387–394, 2016. ISSN 0169-4332. URL <https://www.sciencedirect.com/science/article/pii/S0169433216315446>.
- [65] Jill Chastain. Handbook of x-ray photoelectron spectroscopy.
- [66] Graham. Beamson and David R. Briggs. High resolution xps of organic polymers: The scienta esca300 database. 1992. URL <https://api.semanticscholar.org/CorpusID:92946956>.